Computers in Biology and Medicine 108 (2019) 111–121

Contents lists available at ScienceDirect

Computers in Biology and Medicine

journal homepage: www.elsevier.com/locate/compbiomed

Development of an innovative technology to segment luminal borders of intravascular ultrasound image sequences in a fully automated manner

Abouzar Moshfegh[a,b,*], Ashkan Javadzadegan[a,b,1], Maryam Mohammadi[a], Lakshitha Ravipudi[c], Shaokoon Cheng[d], Ralph Martins[a,e]

[a] Faculty of Medicine and Health Sciences, Macquarie University, Sydney, NSW, 2109, Australia
[b] ANZAC Research Institute, The University of Sydney, Sydney, NSW, 2139, Australia
[c] School of Aerospace, Mechanical and Mechatronic Engineering, The University of Sydney, NSW, 2006, Australia
[d] School of Engineering, Macquarie University, Sydney, NSW, 2109, Australia
[e] School of Exercise, Biomedical and Health Sciences, Edith Cowan University, Perth, Australia

ARTICLE INFO

Keywords:
intravascular imaging
Real-time lumen detection
Machine learning
Fully automated analysis

ABSTRACT

Although intravascular ultrasound (IVUS) is the commonest intravascular imaging modality, it still is inefficient for clinical use as it requires laborious manual analysis. This study demonstrates the feasibility of a near real-time fully automated technology for accurate identification, detection, and quantification of luminal borders in intravascular images. This technology uses a combination of the novel approaches of a self-tuning engine, dynamic and static masking systems, radar-wise scan, and contour correction cycle method. The performance of the computer algorithm developed based on this technology was tested on a sequence of IVUS and True Vessel Characterization (TVC) images obtained from the left anterior descending (LAD) artery of 6 patients with coronary artery disease. The accuracy of the algorithm was evaluated by comparing luminal borders traced manually with those detected automatically. The processing time of the developed algorithm was also tested on a Dell laptop with an Intel Core i7-8750H Processor (4.1 GHz with 6 cores, 9 MB Cache). Linear regression and Bland-Altman analyses indicated high correlation between manual and automatic tracings ($Y = 0.80 \times X + 1.70$, $R^2 = 0.88$ & 0.67 ± 1.31 (bias ± SD)). Whereas analysis of 2000 IVUS images using one CPU core with a 30% load took 23.12 min, the same analysis using six CPU cores with 90% load took 1.0 min. The performance, accuracy, and speed of the presented state-of-the-art technology demonstrates its capacity for use in clinical settings.

1. Introduction

Myocardial infarction, commonly known as a heart attack, is predominantly caused by the rupture of atherosclerotic plaques. Hence, the detection of plaques is vital for early diagnosis and preventive measures [1] for coronary artery disease. Although angiography is widely considered the gold standard in evaluating the functional significance of atherosclerosis, it is unable to characterize atherosclerotic plaques and thereby identify vulnerable plaques prone to rupture [2,3].

Various intravascular imaging modalities have been developed to provide detailed information on the characteristics and composition of atherosclerotic plaques. Intravascular ultrasound (IVUS) is the commonest intravascular imaging technique, which works on the basis of emitting ultrasound pulses and receiving the reflected ultrasound echoes to form a cross-sectional image of a vessel of interest [4,5]. Optical coherence tomography (OCT) has recently been developed as an optical analogy of IVUS that works based on the light emitted from an OCT probe [6,7]. By virtue of systematic differences, OCT provides higher axial and lateral resolution and engenders less noise, allowing visualization of tissue micro-components that are invisible to IVUS. As opposed to IVUS, however, the primary drawback of OCT is its limited tissue penetration, which prevents detailed imaging of the media and adventitia tissue regions [8]. Thus IVUS and OCT provide complementary information to angiography, also providing real-time information on vessel wall morphology and plaque composition [9].

The conventional analysis of IVUS images requires manual processing of images in aspects such as drawing luminal and medial-adventitial borders. Non-automated methods of border detection are not

---

[*] Corresponding author. Faculty of Medicine and Health Sciences, Level 1, 75 Talavera road, Macquarie University, NSW, 2109, Australia.
E-mail address: abouzar.moshfegh@mq.edu.au (A. Moshfegh).

[1] Joint first authors.

https://doi.org/10.1016/j.compbiomed.2019.03.008
Received 10 October 2018; Received in revised form 9 March 2019; Accepted 9 March 2019

only laborious to implement but also subject to considerable discrepancies caused by variability between intra- and inter-observer analyses [5,10,11]. Moreover, the typically poor clarity of IVUS images, caused by the lack of homogeneity in tissue composition and the presence of shadows cast by the guidewire, catheter, and regions of calcium plaque, further complicates the analysis of IVUS images, making manual image processing more arduous [11].

To overcome the drawbacks of manual tracing, many automated and semi-automated border detection techniques have been developed, such as texture-based algorithms [12,13], cross-correlation algorithms [14], active contour energy minimization methods [15,16], and geometric deformable model-based approaches [17]. For instance, Brusseau et al. [16] used an automated method for detecting the endoluminal border based on an active contour that evolves until it optimally separates regions with different statistical properties without using a preselected region of interest or initialization of the contour close to its final shape.

For clinical practice, the most attractive image processing techniques are fully automated [18], as they require minimal inputs and are useable by medical professionals during procedures. However, the majority of automated methods available to date rely on initial patterns or initialization contours obtained from longitudinal views of intravascular images. They may require image stabilization to reduce or remove the movement caused by cardiac and respiratory motions. Artifacts including speckle noise, shadowing behind the guide wire, non-uniform rotational distortion, and reverberation can increase the difficulty of border detection in IVUS images [11]. Consequently, clinical applications of fully automated segmentation methods have had limited success and there is still no fully automatic image segmentation algorithm that provides acceptable accuracy and efficacy in a large patient dataset without human interaction in real time. Although a range of intravascular segmentation software is available [19–23], their absolute status in terms of accuracy and real-time performance demands meticulous comparative study.

The current study presents an innovative technology for a near real-time and fully automated delineation of luminal borders in intravascular images. The accuracy of the method is statistically validated with intima segmentations performed by intravascular imaging experts, and the performance and scalability of the algorithm are demonstrated to justify its suitability for clinical applications.

2. Method

Fig. 1 shows a block diagram of the processes required for the automated segmentation of intravascular images. The processes comprised an image preparation stage, masking systems, self-tuning engine, image segmentation processes, feature extraction using radar-wise scan, a contour correction cycle (CCC), double flagging system, and electrocardiogram (ECG) independent cardiac phase identification. These procedures are described in the following.

2.1. Image preparation

A contrast-limited adaptive histogram equalization (CLAHE) method was applied on small rectangular contextual regions (tiles) specified within the image to enhance the contrast intensity [24]. Bilinear interpolation was utilized to eliminate artificially induced boundaries during tile assembly. Image brightness and contrast intensity were re-normalized by applying the following equation on the greyscale image matrix [I]:

$$[I^{new}] = \frac{([I]^{pow} - Bmin)}{(Bmax - Bmin)} \times 255 \tag{1}$$

where Bmin and Bmax are respectively the smallest and largest elements in the image matrix [I], and pow takes scalar values above unity. Moreover, a *k*th order statistic filter was implemented on the image matrix to reduce “salt and pepper” noise and speckle noise [25,26].

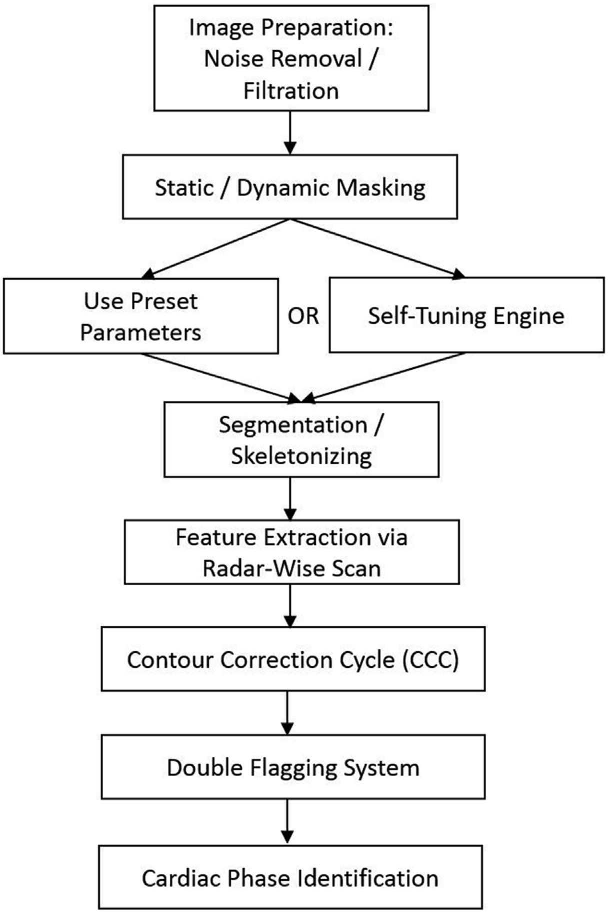

Fig. 1. General workflow to process images for vascular luminal borders.

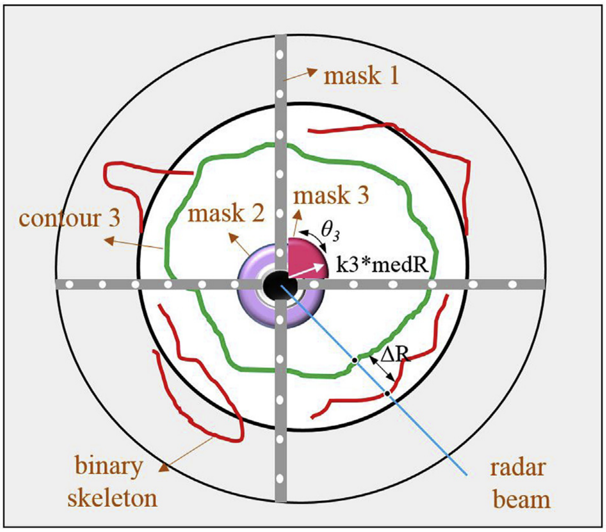

Fig. 2. Schematic representation of structure of static and dynamic masking systems.

2.2. Smart masking systems

Three masking systems (one dynamic and two static masks) were introduced to remove image artifacts cast by the guidewire, catheter, and regions of calcified plaque within the blood vessel. As shown

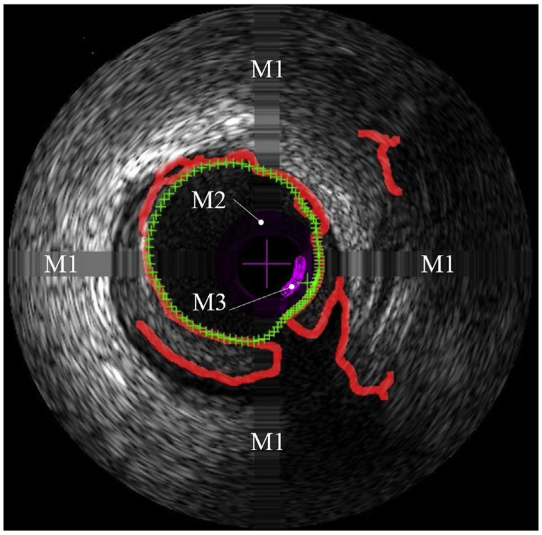

Fig. 3. Binary skeletons detected on a sample IVUS frame as well as the finalized Contour 3 shown by green (+) markers.

schematically in Fig. 2, the first static mask (mask 1) was utilized to attenuate the regular dot points originally present in most of the intravascular images. Mask 1 covered individual white dot points by assigning dot shapes a slightly larger margin to fully cover the dot points. The averaged contrast intensity inside each of the individual rectangular masks was calculated by excluding the pixels within the white dots. Then, the averaged values were assigned to the whole rectangular mask region to attenuate the presence of white dots. The outcome of this masking system is illustrated by "M1" on a representative IVUS image in Fig. 3.

The second static mask (mask 2) was used to attenuate imaging artifacts in the form of bright rings around the catheter caused by signal reverberation. An integrated ring-shaped region of interest was created and targeted around the catheter. It had an internal radius that moved up to a predefined and adjustable external radius within the blood, shown schematically by a purple circle in Fig. 2. This external radius was set *a priori* for a specific imaging modality and catheter type, although it remained relatively constant across various catheters in one imaging modality. Then, the defined circular region was divided into a number of thinner sub-rings of a certain thickness, and pixel texture similar to that of the blood was assigned to each sub-ring. The overall contrast intensity of the texture within each sub-ring was then assigned by linearly extrapolating the blood texture outside the main ring

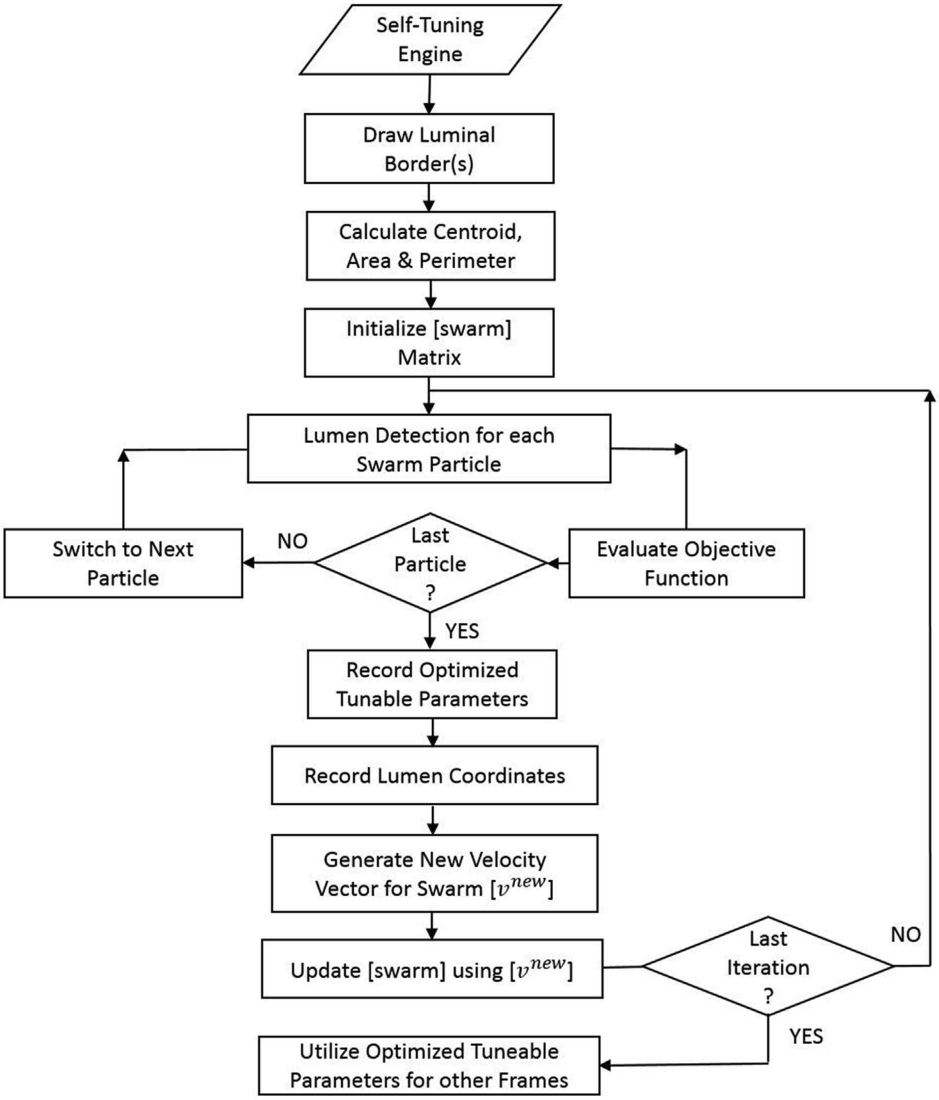

Fig. 4. Workflow to perform self-tuning of parameters using machine learning and PSO method.

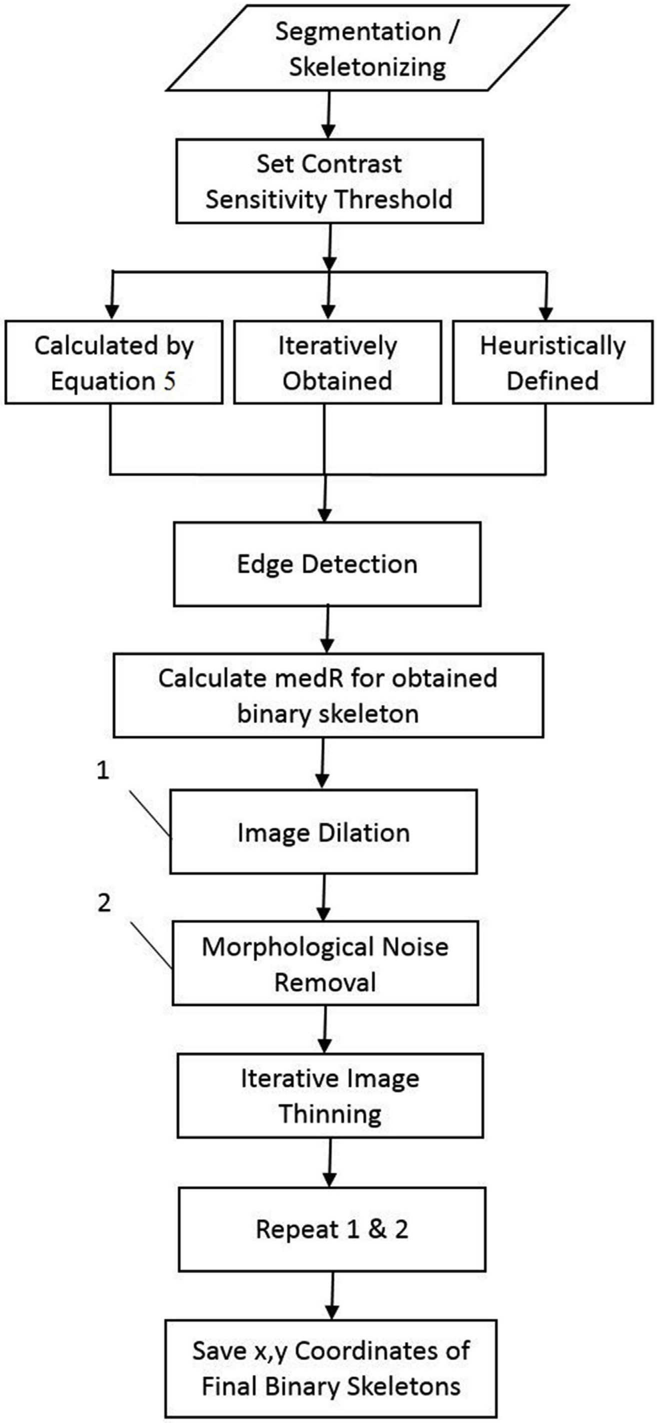

Fig. 5. Workflow to perform image segmentation and skeletonizing.

through to the edge of the catheter. The outcome of this masking system is illustrated by “M2” in Fig. 3.

A dynamic mask (mask 3) was implemented before static mask 2, to attenuate the moving sector of bright spikes and shadows caused by the guidewire shadowing and signal reverberation. It formed a sector-shaped region of interest with the radius of (k_3 * medR) and angle of θ_3, shown schematically in Fig. 2. The k_3 and θ_3 are adjustable factors and medR is a defined metric to characterize the skeleton's morphology obtained via a skeletonizing step (Fig. 1), as determined for each frame after masking and image segmentation. The medR factor was formulated as the median radius of the centroids for each continuous skeleton (or red trace as in Fig. 3). The sector of mask 3 was rotated dynamically around the catheter center through the imaging sequence, to track and chase the brightest point within the region of interest, so that the sector orientation was adjusted by passing its centerline through the brightest point. Masking protocols similar to those used for static mask 2 were also implemented for dynamic mask 3, but only the sub-rings were cut to fit the sector shape. The outcome of this masking system is illustrated by “M3” in Fig. 3.

2.3. Self-tuning engine

A state-of-the-art machine learning technology combined with a particle swarm optimization method (PSO) [27] was created to optimize the key parameters governing the quality of lumen detection. Tunable parameters of image dilation, matrix size [DxD] for image blurring, and matrix power in re-normalization procedure were chosen as the parameters controlling the quality of lumen detection. PSO was used for adjusting the required parameters for lumen detection. Given N^{PAR} as the number of chosen tuneable parameters for PSO, N as the population of the particles swarm, [xmin] and [xmax] as 1xN^{PAR} vectors respectively storing the minimum and maximum numeric values to set an optimization range for each parameter, the swarm matrix was structured as:

$$[swarm] = \begin{bmatrix} 1 \,\ldots\ldots\ldots\ldots\ldots\ldots\ldots\ldots\, j \ldots\ldots\ldots\ldots\ldots\ldots\ldots N^{PAR} \\ i \ldots\ldots . \left[\dfrac{PAR_j^{max} - PAR_j^{min}}{N * i}\right] + PAR_j^{min} \ldots\ldots \\ N \ldots\ldots\ldots\ldots\ldots\ldots\ldots\ldots\ldots\ldots\ldots\ldots\ldots\ldots . \end{bmatrix} \tag{2}$$

where each row (indexed by i) stores a defined factor of tuneable parameters (indexed by j) for each particle, PAR_j^{min} and PAR_j^{max} respectively refer to the minimum and maximum values of the j^{th} tuneable parameter. This defined factor weighed tunable parameters for each particle based on its order in the swarm with respect to the total swarm population via the equation given in [swarm].

Fig. 4 is a flowchart of processes for the self-tuning engine. It began by reading the image sequence and initial setting parameters in which N^{PAR}, N, $Iter$ were the tunable parameters. Then, the luminal borders for several frames were given and the centroid coordinates (Xc, Yc), area (A), and perimeter (P) of the drawn contour(s) were calculated and saved for later use. The swarm matrix itemized above was initialized based on the number of swarm particles, tunable parameters, and their optimization ranges. Image segmentation, skeletonizing, feature extraction, and a contour correction cycle (CCC) method were used to detect a separate luminal border for each particle. Except for the tunable parameters, the remainder of the initial setting parameters were common to all particles. To compare the newly detected lumen for each particle with the manually drawn one, a function was defined to give a measure of morphological deviation between the detected lumen for each particle and the manually drawn lumen for each frame:

$$Fit = |(Xc - Xc^{ref})| + |(Yc - Yc^{ref})| + |(P - P^{ref})| + |(A - A^{ref})|^{0.5} \tag{3}$$

where Xc, Yc are centroid coordinates, A is area, P stands for perimeter, and manually drawn borders are marked with *ref*. This process continued for all swarm particles until a 1xN^{PAR} vector [Fit] for the current PSO iteration was obtained. The minimum scalar value of the [Fit] vector, as it occurred for only one particle, was found and recorded as well as its corresponding tunable parameters, namely [Opt_PAR] as a 1xN^{PAR} vector and lumen coordinates; the latter was stored only when the minimum value of [Fit] was the lowest of all the processed iterations thus far. Two random NxN^{PAR} matrices named [$rand1$] and [$rand2$] were created to update the [$swarm$] matrix by means of a new velocity matrix [v^{new}] of the same size, defined in the following general form:

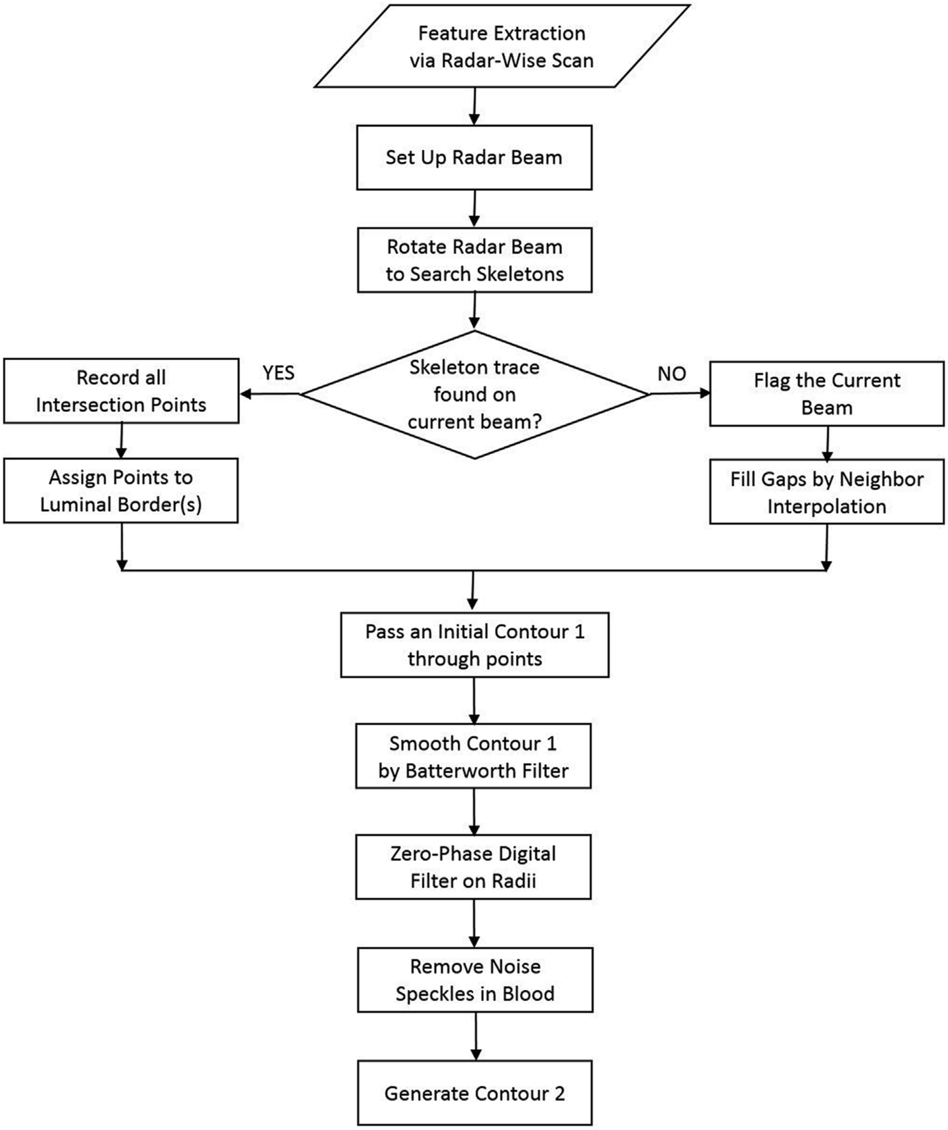

Fig. 6. Workflow for feature extraction using radar-wise scan.

$$\begin{aligned}[v^{new}] &= W \times [v^{old}] + [rand1] \times (\varphi_1 \times ([swarm]^{opt} - [swarm]^{old})) \\ &\quad + \ldots\ldots + [rand2] \\ &\quad \times (\varphi_2 \times (Ones(N, 1) \times [Opt\_PAR] - [swarm]^{old}))[swarm]^{new} \\ &= [swarm]^{old} + [v^{new}] \end{aligned} \tag{4}$$

where scalar W stands for the inertia of a moving population of particles, ϕ_1 and ϕ_2 are self- and social adjustment scalar coefficients set as part of the initial parameter settings, superscripts new/old and opt respectively refer to matrices for the previous/current iteration and the optimized swarm matrix thus far, and $Ones(N, 1)$ is a Nx1 vector with all elements as 1 to create a neighborhood for the optimized particle. $[swarm]^{old}$ was then updated or advanced by adding $[v^{new}]$. Matrices $[v^{new}]$ and $[swarm]^{new}$ were constantly checked and re-normalized if necessary to remain within predefined optimization ranges. Self-tuning processes iterated for *Iter* times, through which only one optimized luminal border(s), with a minimum value of fitness function accompanied by its respective modality- or patient-specific tuned parameters, was obtained to be used for the rest of the frames.

2.4. Image segmentation methods

A set of engineered image segmentation methods was implemented to detect luminal edges or borders using a number of gradient-magnitude algorithms. Depending on the sensitivity thresholds used, this process resulted in binary skeletons of detected edges that could be connected and/or disconnected traces (tracks) that were separately identifiable (see red traces in Fig. 3).

A contrast sensitivity threshold based on the masked images was defined via the following formulation on the grayscale image matrix [I] to arrive at a [2 × 1] vector for sensitivity threshold using:

$$thr = \left[0 \ \left(\frac{mean[I] - \min[I]}{\max[I]} \right) \right] \tag{5}$$

where mean, min, and max are matrix operations to find the average, minimum, and maximum of all matrix elements, and [thr] represents the low/high thresholds for high/low edge sensitivity, to avoid gaps in detected edges. The calculated two-element vector of the sensitivity threshold [thr] was used for the Canny edge detection method [28]. The Canny method searches for local maxima of the gradient of the image matrix, where the gradient is calculated using a derivative of a Gaussian filter. The process began with the low sensitivity results and

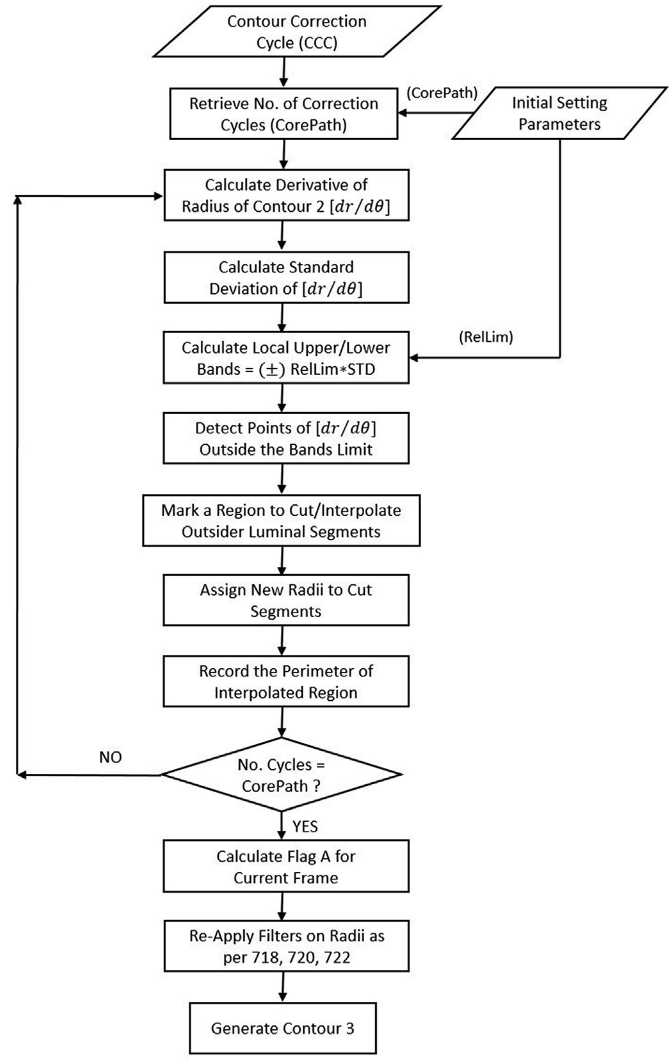

Fig. 7. Workflow to perform contour correction cycle (CCC) method.

then extended to include connected edge pixels from the high sensitivity results, by which means both weak and strong edges were captured, followed by automatic filling of the gaps. The image segmentation and skeletonizing process resulted in binary skeletons of luminal borders in the form of connected and/or disconnected edge traces (tracks), as shown by the red traces in Fig. 3.

A frame-specific morphology metric (medR) was introduced to characterize the distribution, size, and pattern of binary skeletons. First, the radius of curvature centroid (center of line) for each continuous but separated binary track disconnected from the others was measured. Then the median of the measured centroid radii was calculated to arrive at medR.

The general workflow as shown in Fig. 5 began with a preset value of medR as part of the initial setting parameters for the first frame and then calculated medR of the first (or current) frame but utilized it for the second (or next) frame in the masking systems. This was followed by dilation of the binary (or grayscale) intravascular images via morphological operations using rectangular morphological structuring elements utilizing bit packing technology [11], followed by morphological noise removal via area opening techniques in which a flood-fill algorithm was utilized.

Morphological noise removal began by setting the maximum pixel size of noise to be removed. Then the flood-fill algorithm searched (in a reciprocal manner) to assign binary label(s) to all pixels to distinguish those (noises) that belonged to a connected skeletonized component with area less than the above preset value, in order to delete them. This was continued by finite iterations of a thinning morphological operation using square morphological structuring elements [29] until no sensible change occurred in the binary image, and was then concluded by another repeat of dilation and area opening. Finally, the coordinates of the final binary skeleton for the current frame were saved for subsequent use.

2.5. Radar-wise scan

A radar-wise scan technique was developed that created a region of interest with the shape of a radial beam hinged at the catheter center, which rotated with certain angle increment to search for binary skeleton traces belonging to the luminal border of interest.

The initial luminal contour (Contour 1) was smoothed by applying a number of digital filters on radii to generate a secondary smoother luminal contour (Contour 2). Fig. 6 outlines the processes used in the radar-wise scan to assign an initial or temporary luminal contour (Contour 1) to binary skeleton traces. This radial beam was set to begin the search from half of the (k_3 * medR) equivalent to half of the radius of the sector-shaped mask 3 to the maximum radius (maxR) of curvature centroids assigned to skeleton traces [Rc1 Rc2 Rc3 … Rcn]. A program loop then operated to rotate the radar beam with a specified angle increment ($\Delta\theta$) to cover 360°. Non-zero matrix elements or white points of the binary skeleton matrix placed along each radar beam were captured (recorded) with their respective radii and angles through a radial matrix search strategy; these point(s) were at the intersection of radar beam and binary skeleton traces.

Flags labeling each radar beam and interpolation were in place if no point of skeleton trace was found on a particular radar beam, for which the points on neighboring radar beams were circumferentially interpolated and assigned. The closest points to the catheter center were temporarily counted as points on the intima contour.

By connecting the above intersection points, the initial luminal contour generated (Contour 1) was smoothed by applying the low-pass Batterworth infinite impulse response digital filter on radii to obtain a frequency response as flat as possible in the passband to generate a secondary, smoother luminal contour (Contour 2).

Prior to concluding with the smoother Contour 2, a filtration process followed by the introduction of radii data into a zero-phase digital filter [1,4,10] was implemented in both forward and reverse directions (by reversing the filtered sequence) to achieve zero-phase distortion. Subsequently, minimum radii suspected to be noise speckles within the blood were marked and compared against certain criteria and then replaced by interpolated values of neighboring radii.

2.6. Contour correction cycle (CCC)

This is a novel technique that detects and smoothens the relatively sharp (abrupt) variations in luminal border morphology that can be caused by imaging artifacts in the form of either noise speckles in the blood or openings in tissue layers. The CCC also modifies the wall contour where one luminal boundary uncontrollably shifts onto another detected luminal boundary, e.g. when portions of media are mistakenly taken as intima.

As illustrated in Fig. 7, the CCC process began on the current contour by reading in Contour 2 coordinates and the number of contour correction cycles (CorePath) from the initial setting parameters. The process calculated the first derivative of radius [$dr/d\theta$] for points forming Contour 2 where r and θ are radius and angle of each point respectively. The standard deviation of the derivative of radius vector STD = STEDV [$dr/d\theta$] was calculated, where STEDV is an operator to calculate standard deviation.

A preset factor, RelLim > 1, retrieved from the initial setting parameters, was multiplied by the calculated STD and radius of each point (RelLim × STD*r) to generate spatially relative, variable and frame-

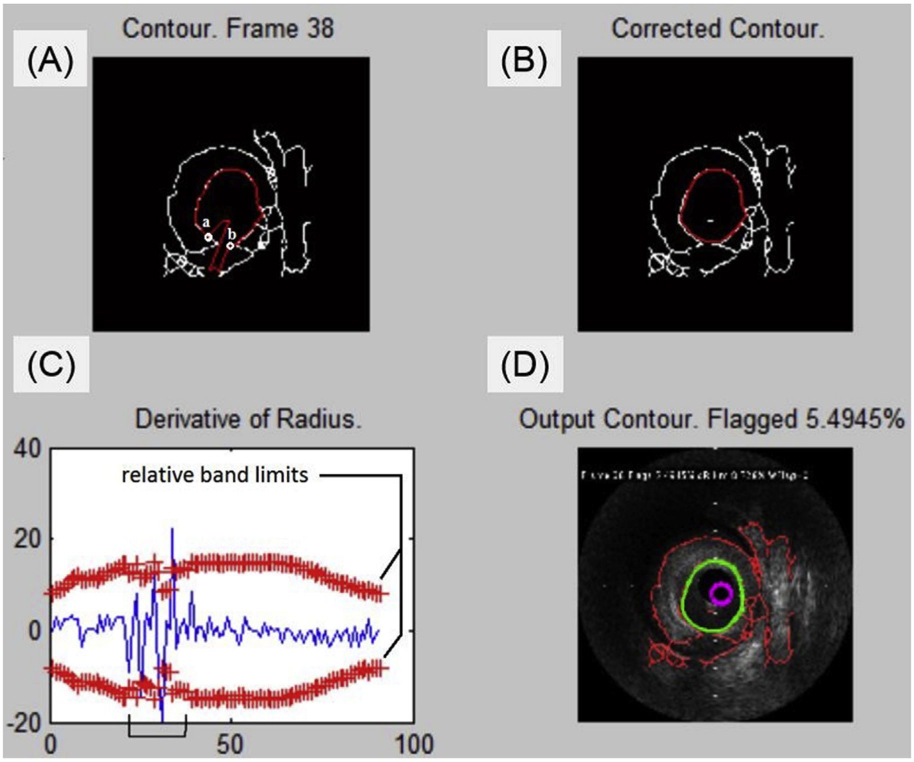

Fig. 8. Major steps in CCC process: (A) Importing Contour 2 to CCC process, (B) plotting derivative of radius versus number of points on Contour 2 bound by relative band limits, (C) Corrected intima contour at the end of CCC process, (D) Contour 3 superimposed on raw TVC intravascular frame showing Flag A.

dependent upper and lower relative band limits. This was done to ensure that abrupt changes in contour morphology were accurately captured.

Upper and lower relative band limits became narrower from one cycle to the next as the contour shape became smoother. Portions of Contour 2 with the derivative of radius outside the relative band limits were marked, including a minor portion of the contour circumference neighboring the marked region as a buffer zone (Fig. 8A). Each marked portion was then cut and replaced via an interpolation method whereby each removed point (j) was assigned a new radius calculated in a weighted manner from Equation (6):

$$r_j^{new} = \frac{r|_{b+dF} - r|_{a-dF}}{\theta|_{b+dF} - \theta|_{a-dF}} \times (\theta|_j - \theta|_{a-dF}) + r|_{a-dF} \tag{6}$$

where (a, b) are the start/end points marking the contour region outside the relative band limits, and dF sets the size of the buffer zone to cut slightly beyond (a, b) points (Fig. 8C). The corrected intima contour is shown in Fig. 8B.

The perimeter of the replaced region at each cycle of the CCC process was measured and recorded to assign Flag A to the current contour by dividing the sum perimeter of the replaced regions through CCC cycles by the total perimeter of the final corrected contour once all cycles (CorePath) terminated at the end of the CCC process. After application of a number of smoothing digital filters, the corrected final Contour 3 was generated (Fig. 8D).

2.7. Double flagging system

This system was used to screen the quality of the generated Contour 3 and to distinguish the correctly detected luminal borders from those prone to inaccuracy. Two flags were assigned to each intravascular frame: Flag A was used to quantify the amount of contour perimeter cut and patched through the CCC technique whereby Contour 2 was advanced to Contour 3; Flag B was introduced to quantify the severity of deviation of the final Contour 3 from the binary skeleton traces by searching via a radar-wise scan.

Fig. 9 outlines a process flowchart for calculating Flag B for a frame in which two search radial ranges ($\Delta R1$, $\Delta R2$) were read from initial setting parameters, such that $\Delta R1 < \Delta R2$. A region of interest (ROI) with the shape of a radial beam hinged at the catheter center rotates by jumping from one point on Contour 3 (Fig. 2, green trace) to another, to search for binary skeleton traces (Fig. 2, red trace) within a certain radial distance ΔR. The search begins from $-\Delta R$ to $+\Delta R$ for each contour point.

For a certain radar beam passing through a point on Contour 3, the method first checked if any skeleton trace existed within the range of $\pm\Delta R1$ around the contour point along the radial beam, then the contour point was moved to a mid-distance between the skeleton trace and the original contour point, followed by giving the point a label of zero as correct. If no point was found within $\pm\Delta R1$ range, the method extended its search scope to within $\pm\Delta R2$ range to label any contour point found within that range with “1” as a possible incorrect contour point; otherwise the contour point was evaluated by the “0” label as correct. This process continued for all the contour points on Contour 3 by shifting the radar beam from one point to another.

Flag B for each contour was then calculated by dividing the summed perimeter of separate portions of Contour 3 covered by points with the label “1” by the total perimeter of Contour 3. After applying a number of smoothing digital filters, an updated Contour 3 was then generated.

2.8. Cardiac phase identification

A fully automated technique was introduced to separate the intravascular frames belonging to end-systolic and end-diastolic cardiac phases, without the need for patient-specific electrocardiogram (ECG) records. The basis of cardiac phase identification involved the periodic or quasi-periodic expansion/contraction of the blood vessel caused by changes in blood pressure through pulse cycles accompanied by vessel deformation. Automatic multiscale-based peak detection (AMPD), based on the calculation and analysis of local maxima, was utilized [30]

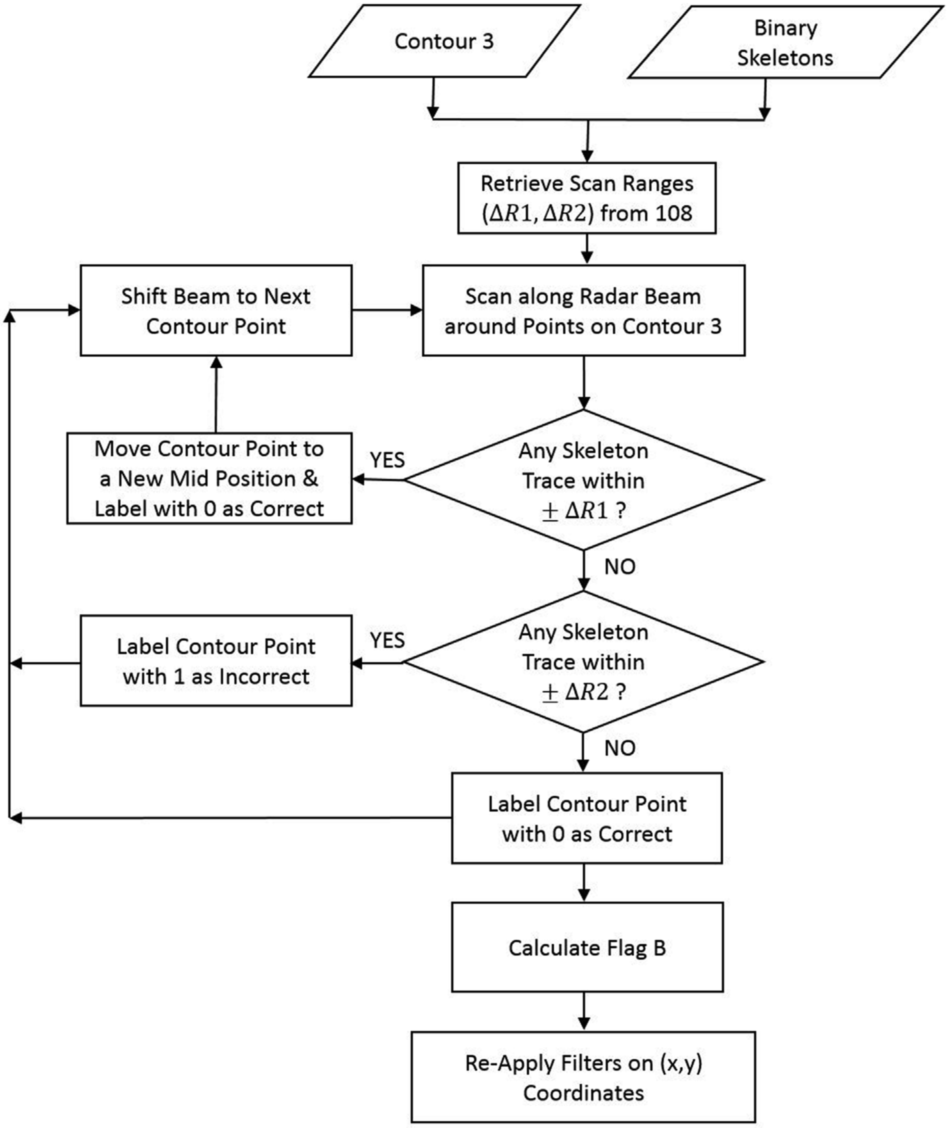

Fig. 9. Workflow to perform double flagging system.

to separate end-diastolic and end-systolic frames on the basis of luminal area variation.

2.9. Study group

The developed algorithm was tested on a sequence of IVUS and TVC images obtained from the left anterior descending (LAD) artery of 6 patients with coronary artery disease. True Vessel Characterization (TVC) is a multimodal intravascular imaging system that fully assembles an IVUS transducer and an optical near-infrared spectroscopy (NIRS) fiber into a single catheter to provide simultaneously co-registered IVUS-NIRS images without a flushing procedure [31]. The IVUS and TVC imaging was performed using the ultrasound systems developed by Volcano therapeutics INC (model Invision TM, IVG-EE) and Infraredx, INC (TVC Insight™, TVC-C195-22). Twenty frames from each patient (total n = 120 frames) were chosen, covering the full arterial length. The accuracy of the results generated by the developed algorithm was quantified by comparing them to the results produced by two imaging experts, who were asked to manually extract the intima borders.

2.10. Statistical analysis

Graphpad Prism v. 5.01 (Graphpad, La Jolla, California) was used to perform the statistical analyses. Linear regression analysis was used to determine the relationship between manually and automatically traced contours. Bland-Altman analysis was also used to compare manually and automatically traced contours.

3. Results

Supplementary video 1 and video 2 show respective examples of the analysis of a series of 3000 IVUS images and 2000 TVC images using the developed algorithm. In these videos, the purple sector-shaped region marked with purple circles (o) and centered around the (+) marker illustrate the dynamic masking system. The red traces are binary skeletons resulting from the image segmentation and skeletonizing processes of luminal border(s) in the form of connected and/or disconnected traces. The green contour is the final Contour 3 fitted onto the red traces.

Supplementary video related to this article can be found at https://doi.org/10.1016/j.compbiomed.2019.03.008.

Fig. 10 compares the luminal segmentation using the developed

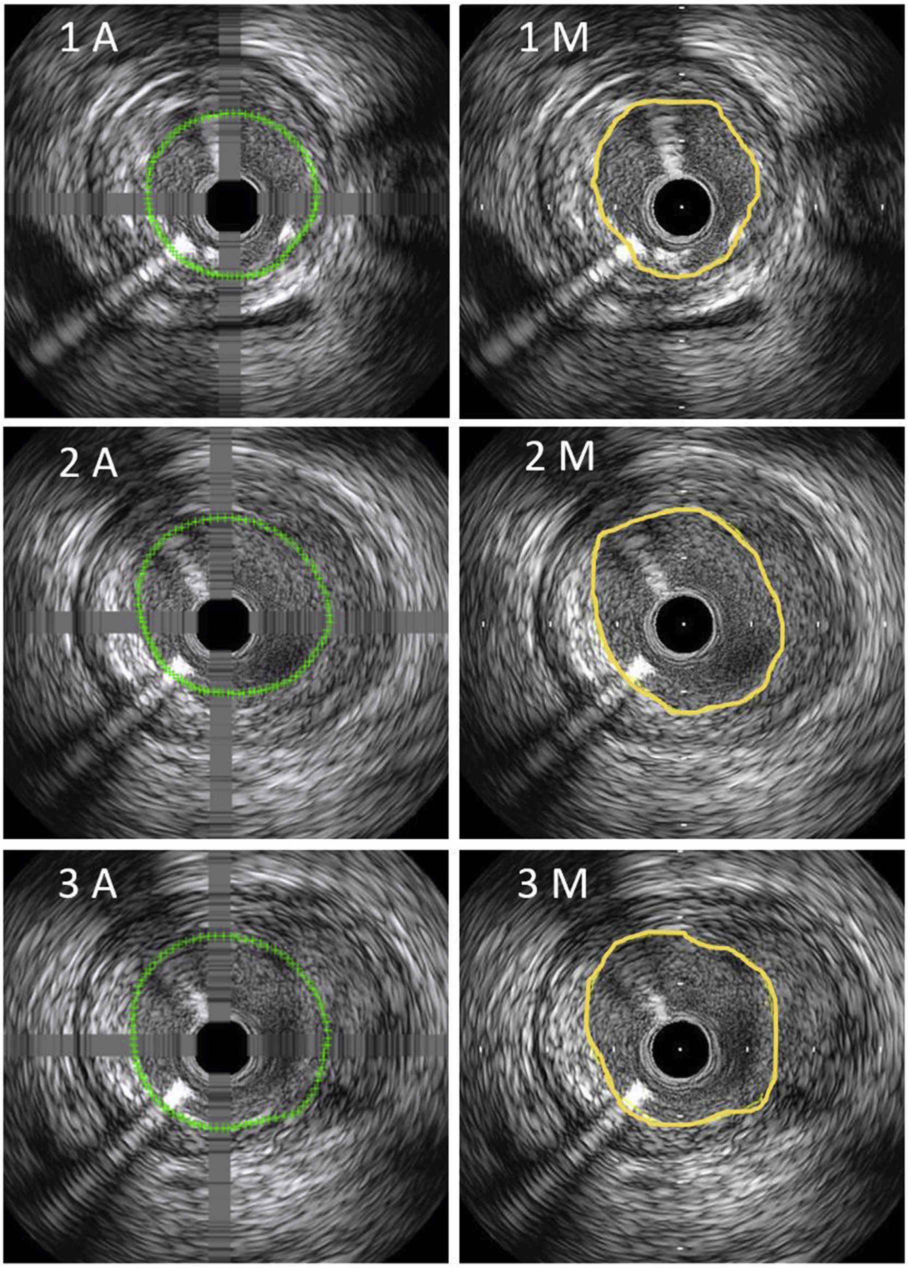

Fig. 10. Visual comparison between automatically (A) and manually (M) traced luminal border of intima layer for 3 representative frames.

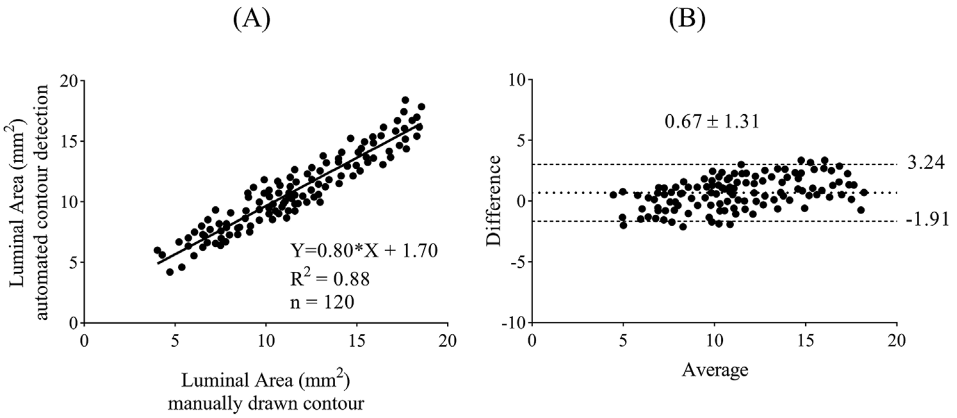

Fig. 11. Comparison between manually and automatically traced luminal borders. (A) Linear regression test, (B) Bland-Altman analysis.

Table 1
Processing time for analysis of 2000 IVUS images without user interaction.

Overall CPUs load %	30	30	30	60	60	60	90	90	90
No. of CPU cores	1	4	6	1	4	6	1	4	6
Processing time (min)	23.12	2.87	2.25	10.25	1.30	1.05	9.75	1.25	1.00

Table 2
Processing time for analysis of 3000 IVUS images without user interaction.

Overall CPUs load %	30	30	30	60	60	60	90	90	90
No. of CPU cores	1	4	6	1	4	6	1	4	6
Processing time (min)	33.87	4.25	3.50	15.62	1.87	1.50	14.13	1.75	1.50

automated method (labeled A) with that manually drawn by imaging experts (labeled M) for 3 representative frames.

Fig. 11A and B illustrate respectively the linear regression analysis and Bland-Altman test between the results of the automated border detection algorithm and the manual border detection by the two experts for the luminal area. As seen, there is an excellent linear relationship between the automated and manual border detections ($R^2 = 0.88$). The bias of the Bland-Altman analysis of the luminal area was 0.67 mm^2 with 95% limits of agreement from −1.91–3.24 mm^2.

The speed of the developed algorithm for detecting luminal borders was tested on a Dell laptop with an Intel Core i7-8750H Processor (4.1 GHz with 6 cores, 9 MB cache) and the results are summarized in Tables 1 and 2. For example, the analysis of 2000 IVUS images using one CPU core with 30% load took 23.12 min, whereas the same analysis using six CPU cores with 90% load took 1.0 min. Similarly, the analysis of 3000 IVUS images using one CPU core with 30% load took 33.87 min, whereas the same analysis using six CPU cores with 90% load took 1.5 min.

4. Discussion

During intravascular imaging, sets of hundreds or even thousands of images are acquired and used as the basis for medical diagnosis. Therefore, the real-time and automatic analyses of intravascular images are important measures to enable efficient and accurate detection of luminal and vessel wall borders [11]. Over the past 20 years, there has been an increase in literature for semi-automatic and automatic IVUS detection technologies such as direct detection of lumen borders, classification of luminal and blood pool areas, and blood speckle noise reduction methods [11]. However, these methods have been only partially successful in the clinical setting and there is as yet no fully automatic image segmentation algorithm that provides sufficient accuracy and efficacy in a large patient database without human interaction [11]. This is mainly due to several inherent artifacts including the presence of guide wire, calcified plaques, side branches, and also the motion of the catheter and the heart [11,32].

In this study, we present an innovative technology based on a combination of novel techniques including smart masking systems, a self-tuning engine, radar-wise scan, and a contour correction cycle that can detect and delineate the luminal borders in IVUS images. We have successfully demonstrated that implementation of the smart masking system can eliminate the imaging artifacts cast by the guidewire, the catheter, and the regions of calcified plaque within the blood vessel. The features that make the presented technology a highly efficient method for analyzing IVUS images are its operation in near real time and its fully automated process that requires minimal to negligible human interaction. The latter feature is advantageous as it reduces intra-observer and inter-observer variability. As a testament to this, the analysis of 3000 IVUS images over 6 CPU cores of a Core i7-8750H Processor @ 4.1 GHz took approximately 90 s. This result indicates the high efficiency of the presented technology for performing in clinical environments where the demand for real-time lumen detection is high. The algorithm is also scalable over multiple CPU or GPU nodes through various parallel processing algorithms.

The technology's high speed facilitates image segmentation of a whole sequence of intravascular frames per patient without skipping, while being independent of contour estimation or initial patterning, aided by the longitudinal view of frame sequences. Linear regression and Bland-Altman analyses also showed good agreement between manual results and results automatically obtained from the technology.

The focus of present study was on detecting the luminal border of the intima layer, a task that is generally challenging due to the high scattering of red blood cells within the lumen, especially when a high-frequency transducer is used [11]. The presented technology also provides a robust foundation for further upgrades to detect media and adventitia borders.

5. Conclusion

The present study has demonstrated the feasibility of a fully automated and real-time computer algorithm to accurately identify and quantify the inner lumen (intima layer) of blood vessels in intravascular images. A variety of novel techniques were incorporated: machine learning from clinically correct luminal boundaries, self-tuning of key segmentation parameters, smart and dynamic masking of imaging artifacts, and innovative feature extraction and contour correction methodologies. This combination made the method near real time and independent of frequent luminal corrections by the user (via longitudinal and/or transverse views), thereby rendering it applicable in clinical settings due to its proven performance, speed, and accuracy.

Future directions

The next step envisaged is evaluation of the proposed methodology by quantitatively rating the accuracy and performance of luminal segmentation via cross-comparison with available software for IVUS and OCT segmentation. A further direction is to upgrade the proposed methodology to segment media and adventitia layers in blood vessels.

Conflict of interest statement

The authors have no conflicts of interest to declare.

References

[1] J.D. Klingensmith, R. Shekhar, D.G. Vince, Evaluation of three-dimensional segmentation algorithms for the identification of luminal and medial-adventitial borders in intravascular ultrasound images, IEEE Trans. Med. Imaging 19 (10) (2000) 996–1011.
[2] C. Berry, et al., Comparison of intravascular ultrasound and quantitative coronary angiography for the assessment of coronary artery disease progression, Circulation 115 (14) (2007) 1851–1857.
[3] T. Takahashi, et al., Intravascular ultrasound and quantitative coronary angiography, Cathet. Cardiovasc. Interv. 55 (1) (2002) 118–128.
[4] D. Gil, et al., Automatic segmentation of artery wall in coronary IVUS images: a probabilistic approach, Computers in Cardiology, IEEE, 20002000.
[5] M.E. Plissiti, et al., An automated method for lumen and media-adventitia border detection in a sequence of IVUS frames, IEEE Trans. Inf. Technol. Biomed. 8 (2) (2004) 131–141.
[6] L.S. Athanasiou, et al., Optical coherence tomography: basic principles of image acquisition, Intravascular Imaging: Current Applications and Research Developments, IGI Global, 2012, pp. 180–193.
[7] A.F. Fercher, Optical coherence tomography–development, principles, applications, Z. Med. Phys. 20 (4) (2010) 251–276.
[8] L. Athanasiou, et al., Currently available methodologies for the processing of intravascular ultrasound and optical coherence tomography images, Expert Rev. Cardiovasc. Ther. 12 (7) (2014) 885–900.
[9] M. Sonka, et al., Segmentation of intravascular ultrasound images: a knowledge-

based approach, IEEE Trans. Med. Imaging 14 (4) (1995) 719–732.
[10] D.S. Meier, et al., Automated morphometry of coronary arteries with digital image analysis of intravascular ultrasound, Am. Heart J. 133 (6) (1997) 681–690.
[11] A. Katouzian, et al., A state-of-the-art review on segmentation algorithms in intravascular ultrasound (IVUS) images, IEEE Trans. Inf. Technol. Biomed. 16 (5) (2012) 823–834.
[12] Dixon, K., et al Characterization of coronary plaque in intravascular ultrasound using histological correlation. in Engineering in Medicine and Biology Society, 1997. Proceedings of the 19th Annual International Conference of the IEEE. 1997. IEEE.
[13] D. Vince, et al., Comparison of texture analysis methods for the characterization of coronary plaques in intravascular ultrasound images, Comput. Med. Imag. Graph. 24 (4) (2000) 221–229.
[14] M. Sonka, et al., Automated segmentation of coronary wall and plaque from intravascular ultrasound image sequences, Computers in Cardiology, IEEE, 19941994.
[15] Z. Luo, Y. Wang, W. Wang, Estimating coronary artery lumen area with optimization-based contour detection, IEEE Trans. Med. Imaging 22 (4) (2003) 564–566.
[16] E. Brusseau, et al., Fully automatic luminal contour segmentation in intracoronary ultrasound imaging-a statistical approach, IEEE Trans. Med. Imaging 23 (5) (2004) 554–566.
[17] A. Taki, et al., Automatic segmentation of calcified plaques and vessel borders in IVUS images, International Journal of Computer Assisted Radiology and Surgery 3 (3–4) (2008) 347–354.
[18] M. Khosrow-Pour, M. Khosrowpour, Encyclopedia of Information Science and Technology vol. 1, IGI Global Snippet, 2009.
[19] QIVUS, Medis medical imaging systems, https://www.medis.nl/products/qivus.
[20] echoPlaque, INDEC medical systems, inc. http://www.indecmedical.com/imed_internal/internalechoplaque.asp.
[21] P.K. Siogkas, et al., *Art Care: A Multi-Modality Coronary 3D Reconstruction and Hemodynamic Status Assessment Software.* Technology and Health Care, (2018), pp. 1–7 Preprint.
[22] VH IVUS imaging, Real-time lesion assessment in the cath lab, https://www.philips.sa/en/healthcare/education-resources/technologies/igt/vh-ivus.
[23] CAAS IntraVascular, Pie medical imaging, https://www.piemedicalimaging.com/product/caas-intravascular/.
[24] K. Zuiderveld, Contrast Limited Adaptive Histogram Equalization, Graphics gems, 1994, pp. 474–485.
[25] R.M. Haralick, L.G. Shapiro, Computer and Robot Vision, Addison-wesley, 1992.
[26] T. Huang, G. Yang, G. Tang, A fast two-dimensional median filtering algorithm, IEEE Trans. Acoust. Speech Signal Process. 27 (1) (1979) 13–18.
[27] J. Kennedy, Particle swarm optimization, Encyclopedia of Machine Learning, Springer, 2011, pp. 760–766.
[28] J. Canny, A computational approach to edge detection, IEEE Trans. Pattern Anal. Mach. Intell. (6) (1986) 679–698.
[29] J.A. Mallery, et al., Assessment of Normal and Atherosclerotic Arterial Wall Thickness with an Intravascular Ultrasound Imaging Catheter, (1990).
[30] F. Scholkmann, J. Boss, M. Wolf, An efficient algorithm for automatic peak detection in noisy periodic and quasi-periodic signals, Algorithms 5 (4) (2012) 588–603.
[31] T. Ma, et al., A review of intravascular ultrasound-based multimodal intravascular imaging: the synergistic approach to characterizing vulnerable plaques, Ultrason. Imag. 38 (5) (2016) 314–331.
[32] H.-B. Park, et al., Clinical feasibility of 3D automated coronary atherosclerotic plaque quantification algorithm on coronary computed tomography angiography: comparison with intravascular ultrasound, Eur. Radiol. 25 (10) (2015) 3073–3083.